Highly Ductile and Ultra-Thick P-Doped FeSiB Amorphous Alloys with Excellent Soft Magnetic Properties

Zongzhen Li [1,2], Shaoxiong Zhou [1,2,*], Guangqiang Zhang [1,2] and Wei Zheng [3]

[1] Advanced Energy & Materials Research Institute Co., Ltd., Changzhou 213000, China;
    zongzhenli@hotmail.com (Z.L.); zhangguangqiang@atmcn.com (G.Z.)
[2] Central Iron & Steel Research Institute, Advanced Technology & Materials Co., Ltd., Beijing 100081, China
[3] Institute for Advanced Materials and Technology, University of Science and Technology Beijing,
    Beijing 100083, China; zhengwei@atmcn.com
[*] Correspondence: sxzhou@atmcn.com; Tel.: +86-0519-8399-9985

check for updates

Abstract: Herein, we demonstrate the successful synthesis of novel $Fe_{80}Si_9B_{(11-x)}P_x$ ($x = 0$, 1, 3, 5, 7) ultra-thick amorphous ribbons by planar flow casting. The influence of P alloying on glass forming ability (GFA), microstructure, thermal stability, soft magnetic properties, and ductility has been systematically investigated. The results reveal that introduction of P into $Fe_{80}Si_9B_{11}$ alloy can remarkably enhance the GFA and increase critical thickness (t_c) of the alloy from 45 to 89 um. Furthermore, the annealed FeSiBP amorphous alloys exhibited excellent soft magnetic properties, including high saturation magnetic flux density of 1.54 T, the low coercivity of 1.5 A/m, and low core losses of 0.15 W/kg. In addition, the representative $Fe_{80}Si_9B_8P_3$ ultra-thick amorphous alloy demonstrate excellent ductility even after annealing at 400 °C for 10 min, which indicates the superior performance of P-doped FeSiB alloys as compared to the commercial $Fe_{78}Si_9B_{13}$ (Metglas 2605 S2) alloy. The combination of high GFA, excellent ductility, and low core losses of newly developed FeSiBP amorphous soft magnetic alloys makes them attractive candidates for magnetic applications in the high-frequency and high-speed electric devices.

Keywords: amorphous alloys; microstructure; soft magnetic properties; bending ductility

1. Introduction

With the development of science and technology, much effort has been devoted to making devices faster, lighter, and more energy efficient, which would make life easier or be more environmentally friendly [1–5]. The energy efficiency of various power electronic devices, such as transformers [5], electric vehicle [6], high-frequency, and advanced high-speed motors [7], could be significantly improved by using newly developed amorphous magnetic cores. The amorphous soft magnetic alloys do not possess crystal-like periodicity and symmetry and simultaneously exhibit superior mechanical characteristics, high corrosion resistance, and excellent soft magnetic properties [8]. Up to now, novel soft magnetic materials have been applied in many fields, such as energy storage, energy conversion, filtering, power generation, and sensing. It has been demonstrated that the replacement of conventional magnetic cores by amorphous soft magnetic cores in distribution transformers, used in electricity networks, can reduce no-load losses by more than 80% [9,10].

Despite the fact that silicon steel is the most commonly used soft magnetic material for motors, high power conversion, and distribution transformers, it exhibits a large amount of core losses at high-frequency for advanced high-speed devices. It has been reported that core losses results in substantial temperature rise and deteriorates the device performance [11]. Regarding core losses,

amorphous materials possess higher electrical resistivity, when compared with silicon steels, and much less ribbon thickness of about 20 μm fabricating by using planar flow casting [12,13]. Hence, amorphous soft magnetic materials demonstrate lower core losses over a wide range of frequency. With the increasing demand for high-efficiency devices, the amorphous soft magnetic alloys have garnered significant research attention and have shown the ability to effectively reduce energy conversion loss. Generally, the wound amorphous soft magnetic cores, which are used in distribution transformers, have a flat geometry with a larger diameter and smaller axial length, which are easy to manufacture and require less cutting [14,15]. However, wound cores imply relatively high core losses and reduction of these core losses require further cutting. Moreover, wound cores are not suited for further applications as complex shaped magnetic components based upon these novel materials [16,17]. The geometrical optimization by cutting significantly enhances the power density when compared to the equivalent silicon steel components. However, the brittleness and relatively small thickness of conventional Fe-based amorphous soft magnetic alloys limit the potential applications and raise the technical challenges in manufacturing processes [13,18,19]. Therefore, the amorphous soft magnetic alloys with high thickness and better ductility should be developed for the successful realization of low-loss electrical devices.

The firstly commercial $Fe_{78}Si_9B_{13}$ (Metglas 2605 S2) amorphous alloy is widely used in distribution transformers due to its excellent combination of low raw material cost and excellent soft magnetic properties, such as low coercivity, high saturation magnetization, and low core losses. $Fe_{80}Si_9B_{11}$ (Metglas 2605 SA1) amorphous alloy was further developed subsequently, and the saturation magnetization was increased from 1.42 to 1.56 T [5,20]. However, the relatively poor glass forming ability (GFA) and fragility, after annealing, limits their potential applications. It has been reported that minor alloying is an effective technique to improve the GFA of Fe-based amorphous alloys [21–24]. More recently, Chang et al. have reported that incorporation of phosphorous (P) into Fe–Si–B alloys effectively enhanced the GFA of $Fe_{76}Si_9B_{10}P_5$ alloy, which resulted in the casting of the $Fe_{76}Si_9B_{10}P_5$ glassy rod with a critical diameter of 2.5 mm by conventional copper mold casting [25]. The excellent GFA of this newly developed Fe-based amorphous alloy opens up avenues for further research for the development of thick amorphous soft magnetic ribbons. As a matter of fact, the development of Fe-based amorphous alloys with excellent ductility, high strength, enhanced GFA, and desirable soft magnetic properties is challenging and vitally important for a wide range of applications. Moreover, after some pioneer studies, a large number of Fe-based bulk amorphous alloys have been synthesized mainly by copper mold casting [26–28]. Unfortunately, the reports on Fe-based ultra-thick amorphous ribbons are rare and the influence of minor-element alloying on ductility, core losses, and soft magnetic properties has not been explored in detail yet. The thermal stability of amorphous alloys must be considered for practical applications because of their tendency to transform from metastable states into more stable states when they are supplied with the necessary thermal energy [29–31]. Annealing is a common way of introducing this transformation of amorphous alloys, and their soft magnetic properties could be greatly improved by suitable annealing [32–34]. Herein, we have demonstrated the effects of P alloying and annealing on $Fe_{80}Si_9B_{(11-x)}P_x$ (x = 0, 1, 3, 5, 7) alloys and systematically evaluated the GFA, thermal stability, soft magnetic properties, and ductility of newly developed FeSiBP ultra-thick amorphous ribbons.

2. Materials and Methods

2.1. Materials and Sample Preparation

The high-purity metals, such as Fe (99.99 wt.%), Si (99.99 wt.%), B (99.99 wt.%), and pre-alloyed Fe_3P (99.9 wt.%) were used in this study. The schematic formation process for the $Fe_{80}Si_9B_{(11-x)}P_x$ (x = 0, 1, 3, 5, 7) amorphous soft magnetic alloys is illustrated in Figure 1. Alloy ingots, with the nominal composition (in at.%) of $Fe_{80}Si_9B_{(11-x)}P_x$ (x = 0, 1, 3, 5, and 7), were firstly prepared by the induction melting of a mixture of the high-purity metals in a Zr-gettered high-purity argon atmosphere.

Subsequently, continuous $Fe_{80}Si_9B_{(11-x)}P_x$ (x = 0, 1, 3, 5, 7) amorphous ribbons, with a width of 5 mm and a thickness of 25–90 μm, were produced through planar flow casting under atmospheric conditions. Finally, the ribbons were cut into 8 mm long strips, which were further annealed in a vacuum furnace and subsequently quenched in water.
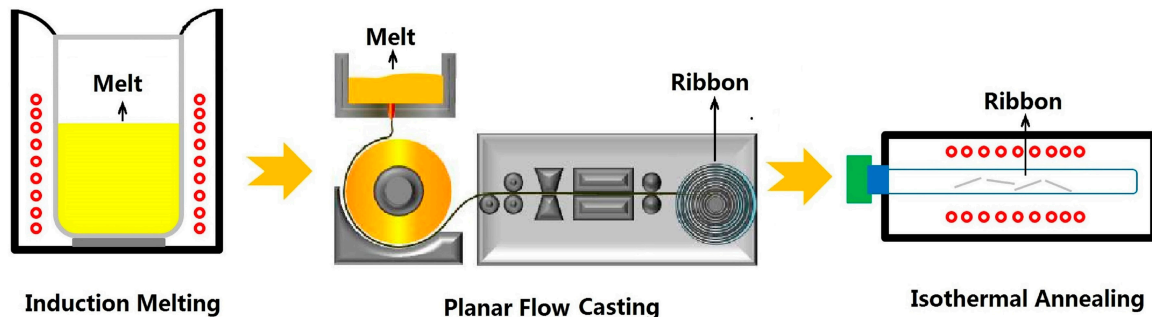

Figure 1. The schematic formation process for the $Fe_{80}Si_9B_{(11-x)}P_x$ (x = 0, 1, 3, 5, 7) amorphous soft magnetic alloys.

Each run was carried out by melting 15 g of the alloy ingots in quartz tubes having rectangular slit of 5 mm × 0.4 mm during the sample preparation processes. The castings were performed with tangential wheel speed from 5 to 50 m/s keeping the other production parameters constant: pressure injection, melt temperature, and the distance between nuzzle and wheel were kept at 400 kPa, 1300 °C, and 2 mm, respectively. The thickness of the melt-spin amorphous ribbons was controlled by changing the tangential wheel speed. The ribbon thickness decreased with increasing wheel speed from ~89 μm, corresponding to 5 m/s down to ~25 μm at 50 m/s for the representative $Fe_{80}Si_9B_{11}$ as-spun ribbons, as illustrated in Figure 2. The ribbon thickness was measured by using an eddy-current coating thickness measurement gauge (HCC-25A).
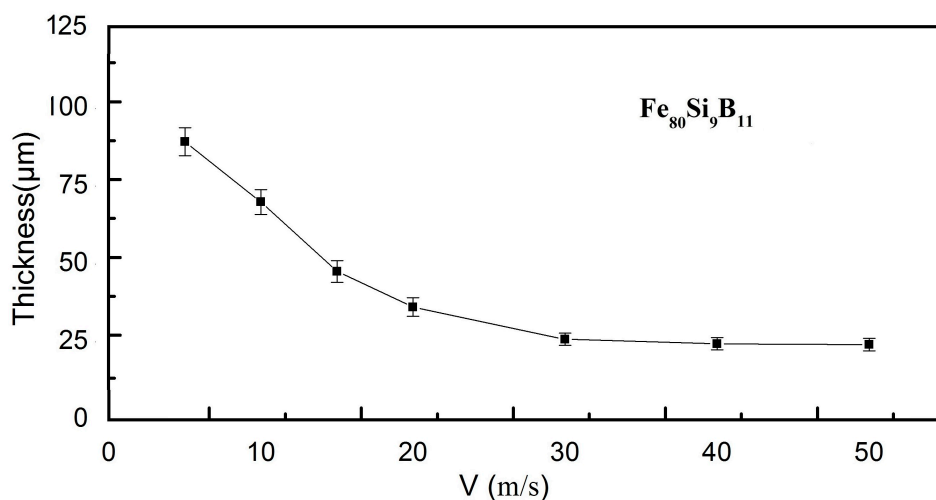

Figure 2. Variation of the thickness for $Fe_{80}Si_9B_{11}$ as-spun ribbons as a function of the tangential wheel speed.

2.2. Characterization Methods

The crystal structure and morphology of the as-spun ribbons were analyzed by using X-ray diffraction (XRD, Bruker D8 Advance, Billerica, MA, USA), with Cu-Kα radiations and high-resolution transition electron microscopy (HRTEM, TECNAI F20, FEI Company, Hillsboro, OR, USA), respectively. The saturation magnetization (B_s) was measured by using a vibrating sample magnetometer

(VSM, Lake Shore 7410, Carson, CA, USA) at a maximum applied field of 800 kA/m. The coercivity (H_c) measurements were carried out by using a DC B-H loop tracer (RIKEN BHS-40, Tokyo, Japan) in a maximum applied field of 800 A/m. The core losses were measured by using an AC B-H loop tracer (Riken, Tokyo, Japan), which was in the frequency range of 50 to 1000 Hz, under the induction of 0.5 to 1 T. The mechanical characterization of the ribbons was carried out by bending the ribbons over the 5-mm mandrels. Bending tests were conducted on the ribbons by bending the ribbons around the mandrels with following diameters, listed in descending order, 20, 15, 10, 5, and 2 mm, according to ASTM Standard E 796-94 [35]. After each bending test, the sample was examined in the SEM for the characterization of shear bands. If the air-side of the ribbon sample did not exhibit shear bands, the process was performed repeatedly on the same sample, using another mandrel with a slightly smaller diameter, until the ribbon sample fractured or permanent deformation via shear band was detected on the outer surface. The ability to resist permanent deformation was measured by using Vickers diamond indenter (AKASHI, AVK-A, Tokyo, Japan) with a load of 2 N and a holding time of 5 s. The shear deformation was measured on the air-side of the sample, and surface was examined by using field emission scanning electron microscope (FESEM, FEI-Nova Nano-SEM-450, Hillsboro, OR, USA). All of the measurements were performed at room temperature.

3. Results

3.1. Glass Forming Ability (GFA) Analysis

The effect of P substitution for B on the amorphous forming ability of the $Fe_{80}Si_9B_{(11-x)}P_x$ ($x = 0$, 1, 3, 5, 7) ultra-thick amorphous ribbons has been determined by using critical thickness (t_c). Figure 3a presents the XRD patterns and corresponding critical thickness of as-spun $Fe_{80}Si_9B_{(11-x)}P_x$ alloy ribbons. The XRD measurements were carried out on air-side of the ribbons, where the cooling rate is the lowest. The XRD patterns exhibit broad diffraction spectra without distinct diffraction peaks, which indicates the amorphous nature of as-spun $Fe_{80}Si_9B_{(11-x)}P_x$ alloy ribbons. The XRD patterns of the as-spun $Fe_{80}Si_9B_{(11-x)}P_x$ ($x = 0$, 3) samples, with a thickness of 45 and 65 μm, are presented in Figure 3b for comparison. The broad halo peak demonstrates that both of the alloys exhibit amorphous phase when the thickness is 45 μm. However, when the thickness was increased to 65 μm, some tiny crystalline peaks corresponding to the α-Fe crystalline phase were observed for the alloys with $x = 0$, but the alloy with $x = 3$ still presents the fully amorphous structure. Glass forming ability (GFA) can be defined as the maximum amorphous thickness (for ribbons) or diameter (for rods) of a sample produced via quenching from the liquid state. In general, GFA exhibits an inverse relationship with the critical cooling rate and a direct relationship with the critical thickness of the sample [36]. The critical thickness (t_c) as a function of P content for $Fe_{80}Si_9B_{(11-x)}P_x$ ($x = 0$, 1, 3, 5, 7) melt-spun ribbons is showed in Figure 3c. The critical thickness (t_c) of $Fe_{80}Si_9B_{(11-x)}P_x$ alloy ribbons has shown a direct relationship with P content and found to be 45, 56, 86, 89, and 82 μm for $x = 0$, 1, 3, 5, and 7, respectively. Firstly, t_c slightly increased from 45 to 56 μm with an increase in P content from $x = 0$ to 1. Then t_c increased sharply and reached a value larger than 80 μm for alloys with $x = 3$. Finally t_c kept a larger value high than 80μm with increasing x up to 7. The XRD results demonstrate that optimal P content can significantly enhance the GFA of the as-spun $Fe_{80}Si_9B_{11}$ alloy ribbons.

The microstructure of the as-spun $Fe_{80}Si_9B_8P_3$ sample with a ribbon thickness of 65 μm was further observed by TEM. The bright-field TEM image does not show any significant feature, as shown in Figure 4a, which is typical of an amorphous material. Moreover, the HRTEM image did not show the lattice fringes (Figure 4b), confirming the amorphous nature of the as-prepared sample. Furthermore, the corresponding SAED consists of a broad diffraction halo, along with a large faint halo, which further confirms the amorphous character of the as-spun $Fe_{80}Si_9B_8P_3$ sample. Hence, both the XRD and TEM results indicate that the GFA of $Fe_{80}Si_9B_{11}$ alloy has been significantly improved with P doping (3 at.%).

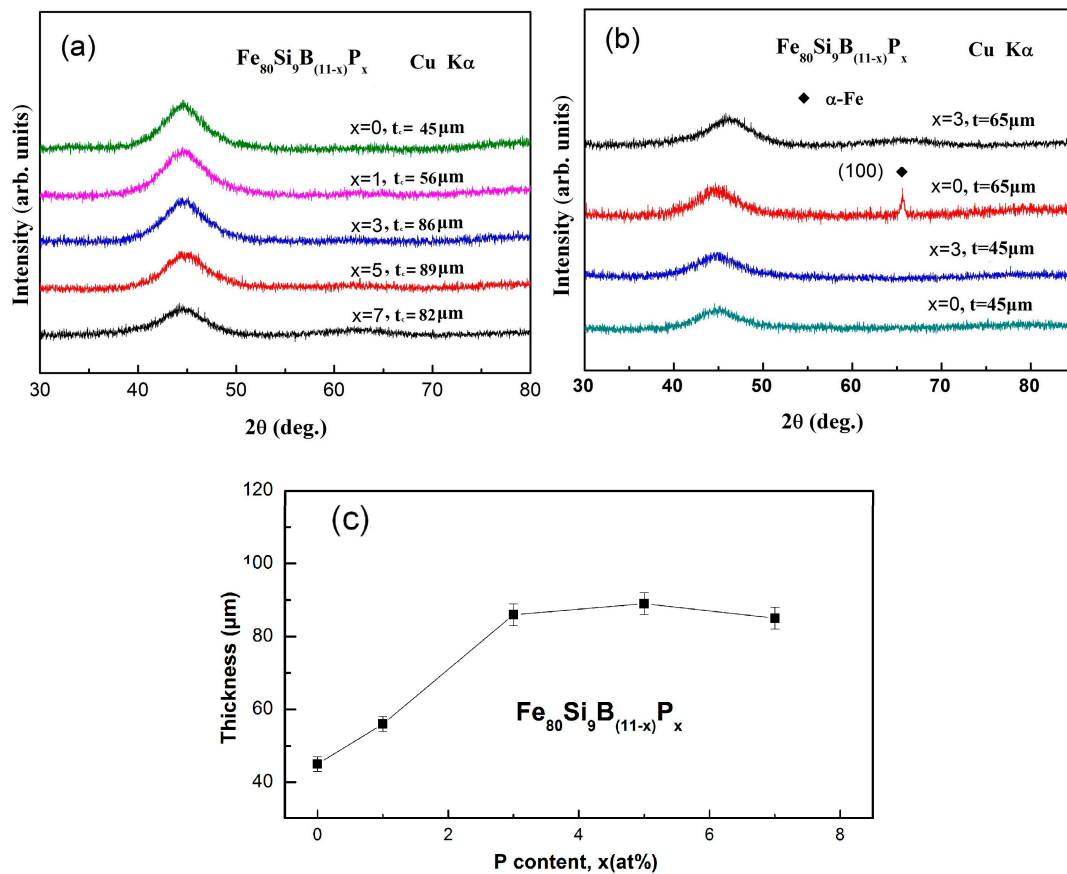**Figure 3.** (**a**) X-ray diffraction (XRD) patterns of the as-spun $Fe_{80}Si_9B_{(11-x)}P_x$ ($x = 0, 1, 3, 5, 7$) amorphous ribbons with critical thickness, (**b**) XRD patterns of melt-spun $Fe_{80}Si_9B_{(11-x)}P_x$ ($x = 0, 3$) amorphous ribbons s with different thickness and (**c**) the variation of critical thickness (t_c) as a function of P content for $Fe_{80}Si_9B_{(11-x)}P_x$ ($x = 0, 1, 3, 5, 7$) melt-spun ribbons.
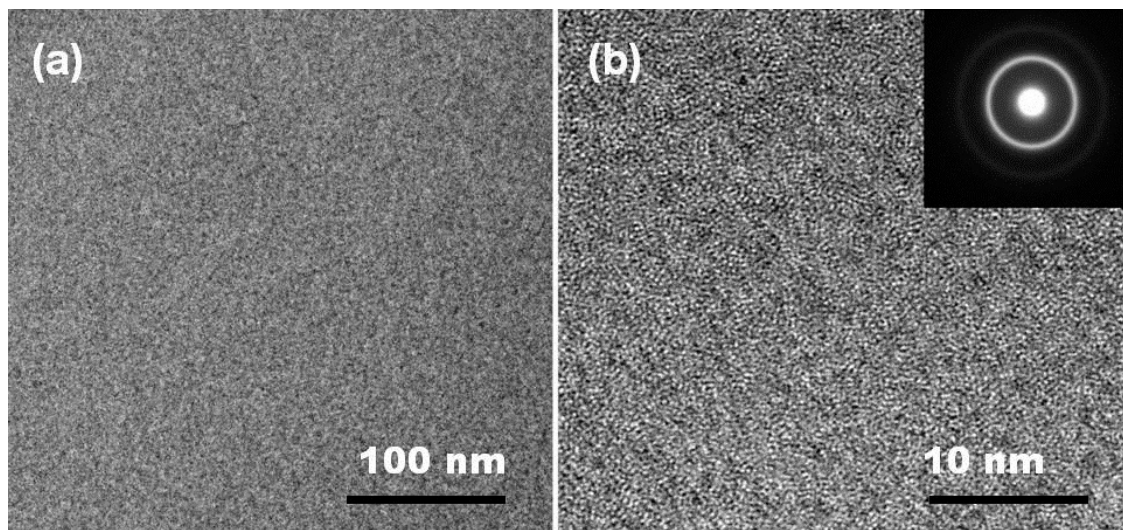

Figure 4. The Bright-filed TEM images (**a**) high-resolution TEM (HRTEM) images and (**b**) corresponding selective area diffraction patterns (inset) of $Fe_{80}Si_9B_8P_3$ sample with a ribbon thickness of 65 μm.

The GFA of an alloy is determined by the composition of the base alloy, purity of the constituents and nature of the alloying additions. It has been reported that atomic size difference and the thermodynamic properties determine the effectiveness of the alloying addition on GFA [24,37]. In the present alloy system, as illustrated in Figure 5a, the mixing enthalpy of Fe-P, Si-P, Fe-B, and Si-B is −31, 0, −11, and 18 kJ/mol, respectively. It is obvious that the introduction of P leads to a larger negative mixing enthalpy, which enhances the GFA of the propose alloy system. On the other hand, P alloying results in higher atomic size mismatches between constituent elements, as shown in Figure 5b, which is also beneficial for GFA of alloy system [36,38,39].
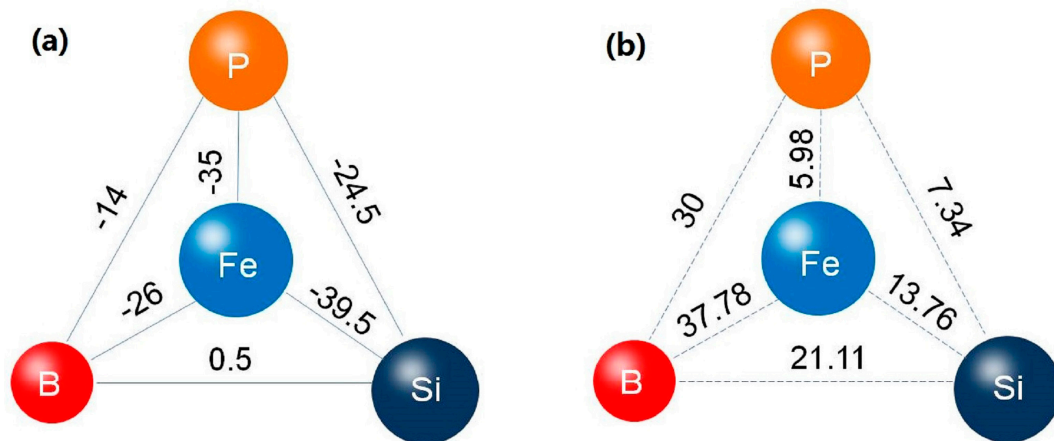

Figure 5. Schematic illustration for the mixing enthalpy (**a**) and mismatch in atomic radius (**b**) for the Fe-Si-B-P alloy system.

3.2. Crystallization Characteristics

The influence of P addition on the crystallization behavior of the as-spun $Fe_{80}Si_9B_{(11-x)}P_x$ (x = 0, 1, 3, 5, 7) amorphous ribbons was also evaluated. DSC curves of all the ribbon samples at a heating rate of 20 K/min in Ar flow is shown in Figure 6. Each sample exhibited no distinct glass transition before crystallization. Two separate exothermic peaks were detected for P-free alloy, indicating that the crystallization occurred in two stages, and the corresponding peaks (marked as "P_1" and "P_2") were located distantly. For the alloys with P alloying another exothermic peak P_3 appeared, leading to the crystallization procedure taken place through three exothermic peaks. With P content increasing from 3 to 7 at.%, the two peaks got closer, which indicated the increase of thermal stability of the supercooled liquid. The deduction was verified by the fully amorphous characteristic in Figure 3 of the $Fe_{80}Si_9B_8P_3$ sample with a ribbon thickness of 65 µm. When compared with the well investigated $Fe_{80}Si_9B_{11}$ alloy, which only could be made into ribbon sample with thickness less than 45 µm, it is strongly confirmed that 3 at.% P element addition can effectively improve the GFA of FeSiBP alloys.
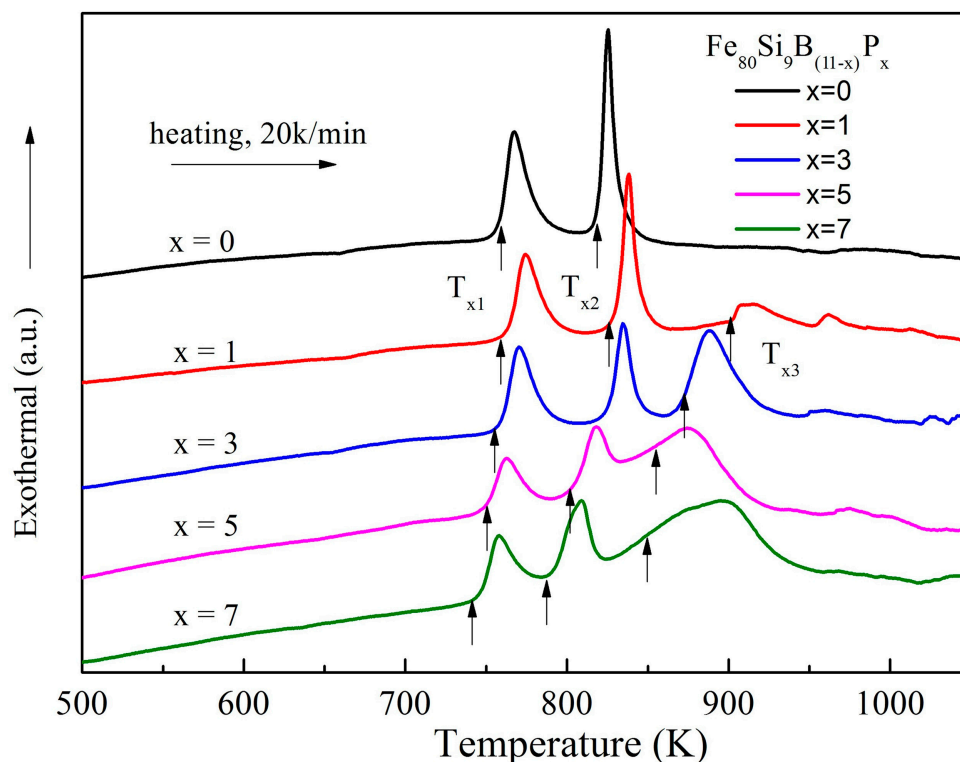
Figure 6. DSC curves of the as-spun $Fe_{80}Si_9B_{(11-x)}P_x$ (x = 0, 1, 3, 5, 7) amorphous ribbons at a heating rate of 20 K/min.

3.3. Soft Magnetic Characteristics

The planar flow casting (PFC) is one of the most promising and commonly used processes for the manufacture of amorphous ribbons. It is well known that the stresses are introduced into as-spun amorphous alloys during rapid casting [40,41]. Being one of the most important soft magnetic parameters coercivity (H_c) is very sensitive to the residual stresses, which can be removed by structural relaxation during annealing. The variation of coercivity (H_c) during annealing reflects the structural relaxation processes in amorphous phase [42–44]. Therefore, the dependence of H_c on annealing temperature (T_a) and annealing time (t_a) for as-spun $Fe_{80}Si_9B_{(11-x)}P_x$ amorphous alloys is systematically studied. Figure 7a presents the relationship between annealing temperature and coercivity when the annealing time is fixed at 10 min. When T_a was increased from room temperature to 380 °C, the H_c gradually decreased due to stress releasing by the structural relaxation of the amorphous alloys. Then, H_c kept almost constant in the temperature range of 380–420 °C, because the amorphous alloys has transformed from metastable states into a more stable state and cast-in stresses during rapid casting has been fully released at this temperature range. However, the H_c value slightly increased up at 440 °C. Hence, an optimal temperature of 400 °C was selected for further experimentation, where minimum H_c value was observed. Figure 7b presents the dependence of H_c on annealing time (t_a), measured at an optimal annealing temperature of 400 °C. The H_c values decreased with the increase of annealing time due to stress relaxation and attained a minimum value of 1.5 A/m after 10 min. Then, the H_c exhibited a little variation with respect to annealing time (t_a) up to 40 min. Therefore, the optimal annealing temperature of 400 °C and an annealing time of 10 min were selected for further experiments.
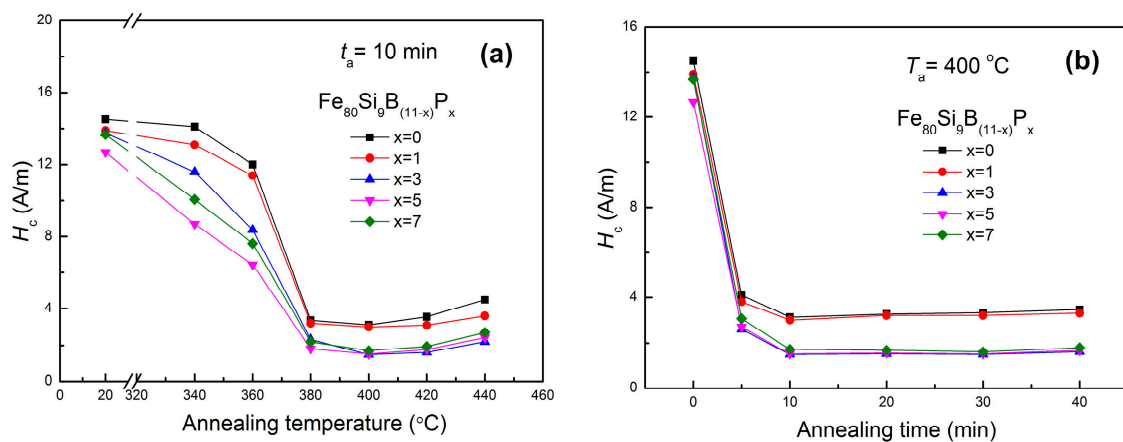
Figure 7. Annealing temperature (T_a) dependence (**a**) and annealing time (t) dependence (**b**) of H_c for $Fe_{80}Si_9B_{(11-x)}P_x$ (x = 0, 1, 3, 5, 7) amorphous alloys.

The dependence of P content on H_c and B_s on $Fe_{80}Si_9B_{(11-x)}P_x$ amorphous ribbons, after annealing under optimal conditions, is shown in Figure 8. First, the H_c values slowly decreased from 3.2 to 3 A/m, with an increase in P content from x = 0 to 1, respectively. Then, the H_c values drastically decreased and reached a minimum value of 1.5 A/m at x = 3 and it remained almost stable up to x = 7. On the other hand, the B_s values monotonically decreased with the increase of P content, which can be attributed to the reduced Fe content with higher P substitution. It should be noted that the minimum value of H_c (1.5 A/m) of the amorphous alloys is much less than the commercial $Fe_{80}Si_9B_{11}$ (Metglas 2605 SA1) alloy. Low H_c favors the application of amorphous alloy core in high frequency and high-speed electrical devices. The enhanced GFA leads to the higher degree of amorphousness, a lesser number of domain wall pinning sites, which result in lower H_c values [45,46]. In summary, the soft magnetic properties of as-spun $Fe_{80}Si_9B_{(11-x)}P_x$ amorphous ribbons can be optimized with optimal annealing conditions and P content.

The core losses will become heat dissipating and deteriorate the efficiency and stability of the magnetic devices. Thus, the core losses of these newly developed Fe-based amorphous alloys should be evaluated before practical applications. The core losses dependence on induction and frequency for conventional silicon steel and $Fe_{80}Si_9B_8P_3$ amorphous alloy is shown in Figure 9a,b. The core losses have shown a direct relationship with induction and frequency for both $Fe_{80}Si_9B_8P_3$ amorphous ribbons and silicon steel. However, the increasing rate of core losses in $Fe_{80}Si_9B_8P_3$ amorphous ribbons is much lower than silicon steel, particularly at high frequency. It is noteworthy that the $Fe_{80}Si_9B_8P_3$ amorphous alloy exhibited extremely low core losses values. The P1.0/50 (core loss at 50 H_Z in 1.0 T induction) for $Fe_{80}Si_9B_8P_3$ amorphous alloy is only 0.15 W/Kg. The dominant losses of magnetic cores are the hysteresis loss, which strongly depends on the H_c. Hence, the $Fe_{80}Si_9B_8P_3$ amorphous alloy can be used in high induction (1.0 T) applications, due to extremely low H_c, high B_s and low core losses. It is worthy to note that such extremely low core losses are uncommon for Fe-based amorphous alloys when compared with previous reports [8,20,25,47]. It has been required to prepare soft magnetic materials with lower core losses, combined with good soft magnetic properties, high-productivity, and low materials cost. Therefore, the present Fe–B–Si–P amorphous alloys are considered to be an important candidate for magnetic core materials.
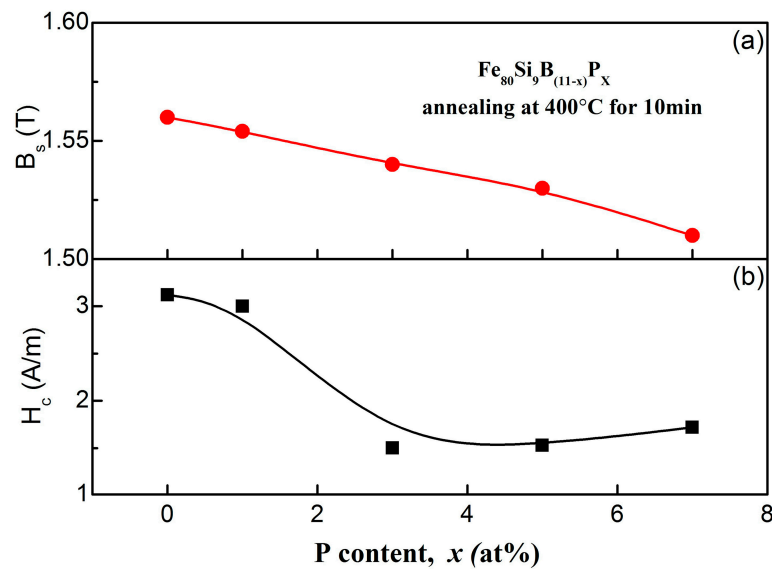
Figure 8. Changes of H_c (**a**) and B_s (**b**) for $Fe_{80}Si_9B_{(11-x)}P_x$ ($x = 0, 1, 3, 5, 7$) amorphous ribbons as a function of P content annealed at 400 °C for 10 min.
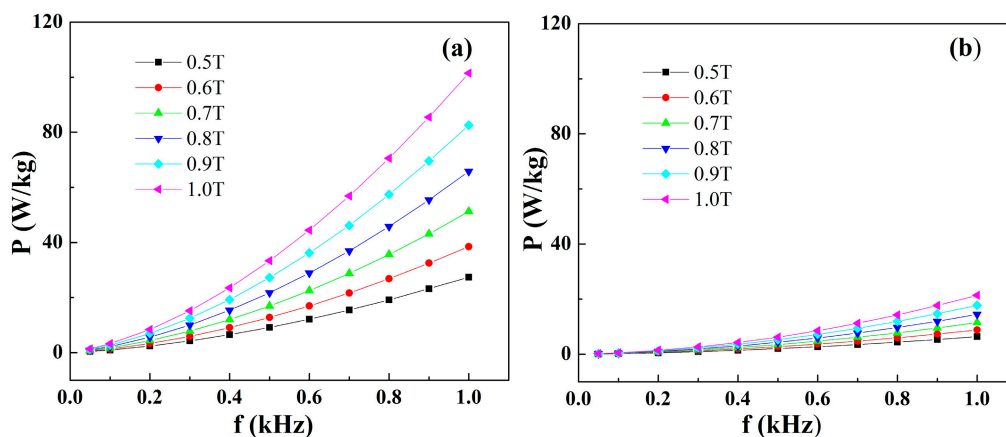

Figure 9. Core losses as a function of frequency in different induction; (**a**) conventional silicon steel (**b**) $Fe_{80}Si_9B_8P_3$ amorphous alloys.

3.4. Microstructural Analysis

In order to further understand the effect of annealing on the variation of coercivity (H_c), The characterized microstructure of the $Fe_{80}Si_9B_{11}$ amorphous ribbons annealed at different temperatures for 10 min is shown in Figure 10. The XRD patterns taken from the air-side of the specimens annealed at 340–420 °C for 10 min are shown in Figure 10a. All of the XRD patterns reveal only a typical halo peak, and no peaks corresponding to crystalline phases, illustrating the amorphous nature of the ribbons after annealing. The $Fe_{80}Si_9B_{11}$ ribbon annealed at 420 °C for 10 min was then subjected to TEM studied. Figure 10b shows its high-resolution TEM (HRTEM) image and the inset is the corresponding selected area electron diffraction (SAED) pattern. The HRTEM image shows a fully random arrangement of atoms, while the diffraction pattern consists of halos. These confirm that the annealed specimen is still fully amorphous. It is well known that glass formation ability (GFA) exhibits a direct relationship with the liquid thermal stability of amorphous alloys. Crystallization phase is more difficult to precipitate for the amorphous alloys with higher glass forming ability. When considering that the representative $Fe_{80}Si_9B_{11}$ amorphous alloy with the lowest GFA still retains its amorphous nature even after annealing at 420 °C for 10 min, it can be safely concluded that all of

the $Fe_{80}Si_9B_{(11-x)}P_x$ samples could preserve amorphous microstructure during the annealing process at 340–420 °C for 10 min. Suitable annealing well below the crystallization point relaxes the structure, maintaining its amorphous character, and resulting in moderate magnetic softening due to the relief of intrinsic cast-in stresses during rapid casting.
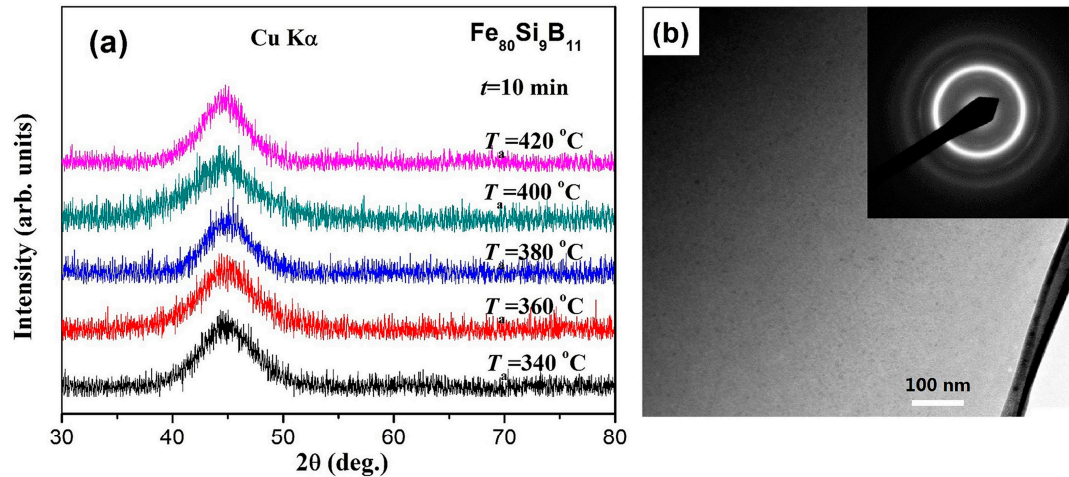

Figure 10. (**a**) X-ray diffraction (XRD) patterns of the as-spun $Fe_{80}Si_9B_{11}$ samples annealed at different temperatures for 10 min; (**b**) The Bright-filed TEM images and corresponding selective area diffraction patterns (inset) of $Fe_{80}Si_9B_{11}$ sample annealed at 420 °C for 10 min.

3.5. Mechanical Characteristics

The mechanical characterization, such as bending ductility and Vickers indentation tests, were carried out to explore the influence of P alloying and annealing conditions on mechanical properties of the representative $Fe_{80}Si_9B_8P_3$ amorphous ribbons. The Mandrel bend testing is illustrated in Figure 11a. Figure 11b,c exhibits the top surface SEM images of as-spun ribbons and samples annealed at 400 °C for 10 min after the bending test, respectively. As shown in Figure 11b, high-density shear bands and the corresponding interactions are visible on the specimen surface of the as-spun amorphous ribbons, implying the ductile nature of the specimen. It is consistent with the excellent bending ductility of as-spun amorphous ribbons, which can be bent to 180° without breaking. After annealing, the number of shear bands was reduced, whereas the inter-shear band spacing became larger, which indicates the reduction in ductility. However, we have not observed any cracks in the annealed $Fe_{80}Si_9B_8P_3$ specimen, which confirms the excellent bending ductility after annealing, as illustrated in Figure 11c.

The indentation testing is illustrated in Figure 12a. The top-view of indentation marks of as-spun ribbons and samples annealed at 400 °C for 10 min, under the load of 2 N and a holding time of 5 s by Vickers indenter, are shown in Figure 12b,c. The Vickers hardness values of the as-cast and annealed $Fe_{80}Si_9B_8P_3$ amorphous ribbons are 970.4 and 950.8 HV, respectively, which are higher than that of the traditional silicon steels and exhibit the excellent wear resistance of prepared alloys [48]. The pile-up feature, near the indentation mark, suggests the inhomogeneous deformation of the samples. It was interesting to observe the numerous shear bands in the pile-up areas, around the hardness indentation marks, in both as-spun and annealed samples, which indicates the excellent deformation ability against indentation. However, the number and appearance of the shear bands, around the indentation marks, were lower and less obvious in annealed samples. The variation in the appearance of the indentation marks demonstrates that annealing reduced the ductility of $Fe_{80}Si_9B_8P_3$ amorphous ribbons. However, the presence of shallow slip-steps markings near the indentation and the absence of obvious cracks indicate that the samples still possess enough elastic-plastic deformation ability.
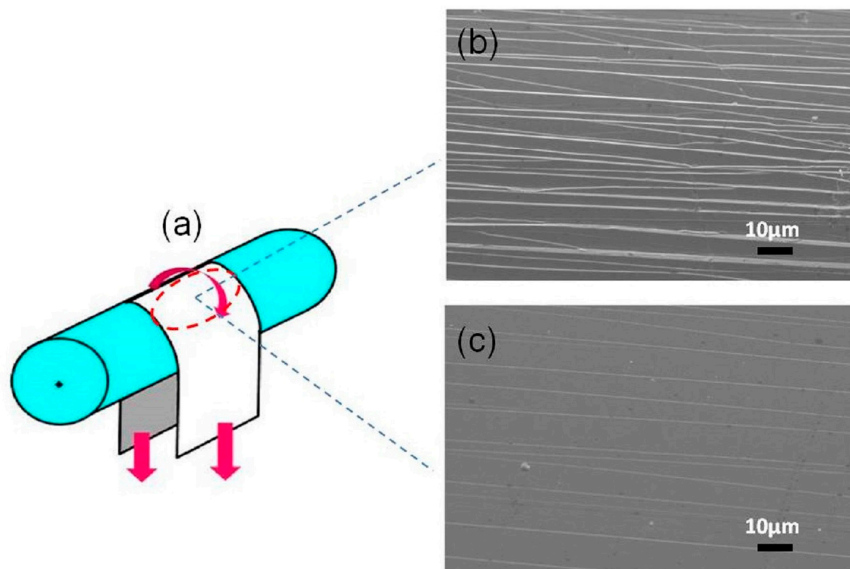
Figure 11. Schematic diagram of the bending test (**a**) and SEM images obtained from the top surface of the bent $Fe_{80}Si_9B_8P_3$ alloy ribbons; (**b**) as-quenched specimen; and, (**c**) annealed at 400 °C for 10 min.

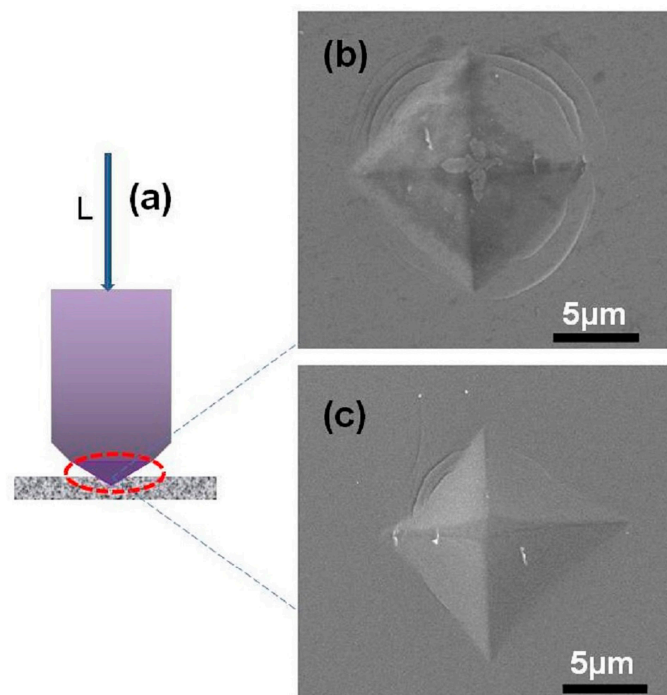**Figure 12.** Schematic diagram of the Vickers indentation testing (**a**) and SEM images of indentation marks of the $Fe_{80}Si_9B_8P_3$ amorphous ribbon; (**b**) as-quenched specimen; and, (**c**) annealed at 400 °C for 10 min.

The atomic packing density is one of the most important factors affecting the ductility of amorphous alloys [49]. In Fe-Si-B-P alloy system, P was introduced as an alloying element and the dominant Fe element has a large atomic size mismatch of 6%, 38%, and 14% with Si, B, and P, respectively, as illustrated in Figure 5b. It has been reported that elements with larger atomic size mismatches can form a highly packed atomic configuration [50,51]. Hence, the incorporation of

smaller size P element led to a much denser atomic packing arrangement, which promotes the slip and interaction of the shear bands and improves the ductility.

4. Conclusions

A comprehensive investigation was carried out to explore the influence of P alloying on glass forming ability (GFA), microstructure, soft magnetic properties, and ductility of $Fe_{80}Si_9B_{(11-x)}P_x$ ($x = 0$, 1, 3, 5, 7) amorphous alloys. The main findings of this study are summarized, as follows:

1. The GFA and soft magnetic properties of as-spun $Fe_{80}Si_9B_{(11-x)}P_x$ amorphous alloys were improved due to the incorporation of a minor amount of P element. However, the excess of P led to the reduction of iron content and the deterioration of saturation magnetization. Hence, an optimal amount of alloying element is required to attain desired properties.

2. The $Fe_{80}Si_9B_{(11-x)}P_x$ amorphous alloys possess superior soft magnetic properties, such as high B_s of 1.54 T low H_c of 1.5 A/m and low core losses of 0.15 W/kg.

3. The representative $Fe_{80}Si_9B_8P_3$ amorphous alloy has exhibited excellent bending ductility and a ductile indentation response, even after annealing at 400 °C for 10 min, which demonstrates the good manufacturability of the as-spun and annealed $Fe_{80}Si_9B_8P_3$.

4. The combination of high GFA, low core losses, and excellent ductility, even after annealing, of FeSiBP ultra-thick amorphous ribbons, make them desirable for the industrial production and utilization as soft magnetic materials.

References

1. Amjad, S.; Neelakrishnan, S.; Rudramoorthy, R. Review of design considerations and technological challenges for successful development and deployment of plug-in hybrid electric vehicles. *Renew. Sustain. Energy Rev.* **2010**, *14*, 1104–1110. [CrossRef]

2. Huang, Q.; Song, Y.; Sun, X.; Jiang, L.; Pong, P.W. Magnetics in smart grid. *IEEE Trans. Magn.* **2014**, *50*, 1–7. [CrossRef]

3. Soinski, M.; Leszczynski, J.; Swieboda, C.; Kwiecien, M. Nanocrystalline block cores for high-frequency chokes. *IEEE Trans. Magn.* **2014**, *50*, 2801904:1–2801904:4. [CrossRef]

4. Leary, A.M.; Ohodnicki, P.R.; McHenry, M.E. Soft magnetic materials in high-frequency, high-power conversion applications. *JOM* **2012**, *64*, 772–781. [CrossRef]

5. Hasegawa, R.; Azuma, D. Impacts of amorphous metal-based transformers on energy efficiency and environment. *J. Magn. Magn. Mater.* **2008**, *320*, 2451–2456. [CrossRef]

6. Simizu, S.; Ohodnicki, P.R.; McHenry, M.E. Metal amorphous nanocomposite soft magnetic material-enabled high power density, rare earth free rotational machines. *IEEE Trans. Magn.* **2018**, *54*, 1–5. [CrossRef]

7. Fan, T.; Li, Q.; Wen, X. Development of a high power density motor made of amorphous alloy cores. *IEEE Trans. Ind. Electron.* **2014**, *61*, 4510–4518. [CrossRef]

8. Lashgari, H.; Chu, D.; Xie, S.; Sun, H.; Ferry, M.; Li, S. Composition dependence of the microstructure and soft magnetic properties of Fe-based amorphous/nanocrystalline alloys: A review study. *J. Non-Cryst. Solids* **2014**, *391*, 61–82. [CrossRef]

9. Okazaki, Y. Loss deterioration in amorphous cores for distribution transformers. *J. Magn. Magn. Mater.* **1996**, *160*, 217–222. [CrossRef]

10. Kolano, R.; Kolano-Burian, A.; Polak, M.; Szynowski, J. Application of rapidly quenched soft magnetic materials in energy-saving electric equipment. *IEEE Trans. Magn.* **2014**, *50*, 2004804:1–2004804:4. [CrossRef]

11. Girgis, R.; Mechler, G.; Zhou, G. Calculation of core hot-spot temperature in power and distribution transformers. *IEEE Trans. Power Deliv.* **2002**, *17*, 991–995.

12. Kefalas, T.D.; Magdaleno-Adame, S. Techno-economic comparative evaluation of mixed and conventional magnetic wound cores for three-phase distribution transformers. *Electr. Power Syst. Res.* **2018**, *155*, 331–339. [CrossRef]

13. Kauder, T.; Hameyer, K. Performance factor comparison of nanocrystalline, amorphous, and crystalline soft magnetic materials for medium-frequency applications. *IEEE Trans. Magn.* **2017**, *53*, 1–4. [CrossRef]

14. Shuai, P.; Biela, J. Influence of material properties and geometric shape of magnetic cores on acoustic noise emission of medium-frequency transformers. *IEEE Trans. Magn.* **2017**, *32*, 7916–7931. [CrossRef]

15. Georgilakis, P.S.; Hatziargyriou, N.D.; Doulamis, N.D.; Doulamis, A.D.; Kollias, S.D. Prediction of iron losses of wound core distribution transformers based on artificial neural networks. *Neurocomputing* **1998**, *23*, 15–29. [CrossRef]

16. Hernández, I.; Olivares-Galván, J.C.; Georgilakis, P.S.; Cañedo, J.M. A novel octagonal wound core for distribution transformers validated by electromagnetic field analysis and comparison with conventional wound core. *IEEE Trans. Magn.* **2010**, *46*, 1251–1258. [CrossRef]

17. Amoiralis, E.I.; Tsili, M.A.; Kladas, A.G. Transformer design and optimization: A literature survey. *IEEE Trans. Power Deliv.* **2009**, *24*, 1999–2024. [CrossRef]

18. Kumar, G.; Ohnuma, M.; Furubayashi, T.; Ohkubo, T.; Hono, K. Thermal embrittlement of Fe-based amorphous ribbons. *J. Non-Cryst. Solids* **2008**, *354*, 882–888. [CrossRef]

19. Niu, Y.; Bian, X.; Wang, W. Origin of ductile–brittle transition of amorphous $Fe_{78}Si_9B_{13}$ ribbon during low temperature annealing. *J. Non-Cryst. Solids* **2004**, *341*, 40–45. [CrossRef]

20. Ogawa, Y.; Naoe, M.; Yoshizawa, Y.; Hasegawa, R. Magnetic properties of high B_s Fe-based amorphous material. *J. Magn. Magn. Mater.* **2006**, *304*, 675–677. [CrossRef]

21. Ma, L.; Inoue, A. On glass-forming ability of Fe-based amorphous alloys. *Mater. Lett.* **1999**, *38*, 58–61. [CrossRef]

22. Li, H.; Kim, K.; Yi, S. Enhanced glass-forming ability of Fe-based bulk metallic glasses prepared using hot metal and commercial raw materials through the optimization of mo content. *Scr. Mater.* **2007**, *56*, 1035–1038. [CrossRef]

23. Wang, W.-H.; Dong, C.; Shek, C. Bulk metallic glasses. *Mater. Sci. Eng. R* **2004**, *44*, 45–89. [CrossRef]

24. Chen, N.; Martin, L.; Luzguine-Luzgin, D.V.; Inoue, A. Role of alloying additions in glass formation and properties of bulk metallic glasses. *Materials* **2010**, *3*, 5320–5339. [CrossRef] [PubMed]

25. Makino, A.; Kubota, T.; Chang, C.; Makabe, M.; Inoue, A. Fe-metalloids bulk glassy alloys with high Fe content and high glass-forming ability. *J. Mater. Res.* **2008**, *23*, 1339–1342. [CrossRef]

26. Li, S.; Wei, Q.; Li, Q.; Jiang, B.; Chen, Y.; Sun, Y. Development of Fe-based bulk metallic glasses as potential biomaterials. *Mater. Sci. Eng. C* **2015**, *52*, 235–241. [CrossRef] [PubMed]

27. Li, H.; Li, C.; Cao, D.; Yang, W.; Li, Q.; Lu, Z. Influences of oxygen on plastic deformation of a Fe-based bulk metallic glass. *Scr. Mater.* **2017**, *135*, 24–28. [CrossRef]

28. Suryanarayana, C.; Inoue, A. Iron-based bulk metallic glasses. *Int. Mater. Rev.* **2013**, *58*, 131–166. [CrossRef]

29. Buschow, K.H.J. Short-range order and thermal stability in amorphous alloys. *J. Phys. F Met. Phys.* **1984**, *14*, 593–607. [CrossRef]

30. Johnson, W.L. Thermodynamic and kinetic aspects of the crystal to glass transformation in metallic materials. *Prog. Mater. Sci.* **1986**, *30*, 81–134. [CrossRef]

31. Luo, W.K.; Sheng, H.W.; Alamgir, F.M.; Bai, J.M.; He, J.H.; Ma, E. Icosahedral short-range order in amorphous alloys. *Phys. Rev. Lett.* **2004**, *92*, 145502:1–145502:4. [CrossRef] [PubMed]

32. Egami, T. Structural relaxation in amorphous alloys—compositional short range ordering. *Mater. Res. Bull.* **1978**, *13*, 557–562. [CrossRef]

33. Li, Z.Z.; Wang, A.D.; Chang, C.T.; Wang, Y.G.; Dong, B.S.; Zhou, S.X. Synthesis of fesibpnbcu nanocrystalline soft-magnetic alloys with high saturation magnetization. *J. Alloys Compd.* **2014**, *611*, 197–201. [CrossRef]

34. Xue, L.; Liu, H.S.; Dou, L.T.; Yang, W.M.; Chang, C.T.; Inoue, A.; Wang, X.M.; Li, R.W.; Shen, B.L. Soft magnetic properties and microstructure of $Fe_{84-x}Nb_2B_{14}Cu_x$ nanocrystalline alloys. *Mater. Des.* **2014**, *56*, 227–231. [CrossRef]

35. Engelmaier, W. A method for the determination of ductility for thin metallic materials. *ASTM Spec. Tech. Publ.* **1982**, *753*, 279–295.

36. Lu, Z.P.; Bei, H.; Liu, C.T. Recent progress in quantifying glass-forming ability of bulk metallic glasses. *Intermetallics* **2007**, *15*, 618–624. [CrossRef]

37. Takeuchi, A.; Inoue, A. Classification of bulk metallic glasses by atomic size difference, heat of mixing and period of constituent elements and its application to characterization of the main alloying element. *Mater. Trans.* **2005**, *46*, 2817–2829. [CrossRef]

38. Senkov, O.N.; Miracle, D.B. Effect of the atomic size distribution on glass forming ability of amorphous metallic alloys. *Mater. Res. Bull.* **2001**, *36*, 2183–2198. [CrossRef]

39. Busch, R.; Schroers, J.; Wang, W. Thermodynamics and kinetics of bulk metallic glass. *MRS Bull.* **2007**, *32*, 620–623. [CrossRef]

40. Srinivas, M.; Majumdar, B.; Phanikumar, G.; Akhtar, D. Effect of Planar Flow Melt Spinning Parameters on Ribbon Formation in Soft Magnetic $Fe_{68.5}Si_{18.5}B_9Nb_3Cu_1$ Alloy. *Metall. Mater. Trans. B* **2011**, *42*, 370–379. [CrossRef]

41. Fiedler, H.; Mühlbach, H.; Stephani, G. The effect of the main processing parameters on the geometry of amorphous metal ribbons during planar flow casting (PFC). *J. Mater. Sci.* **1984**, *19*, 3229–3235. [CrossRef]

42. Axinte, E. Metallic glasses from "alchemy" to pure science: Present and future of design, processing and applications of glassy metals. *Mater. Des.* **2012**, *35*, 518–556. [CrossRef]

43. Li, Z.Z.; Wang, A.D.; Chang, C.T.; Wang, Y.G.; Dong, B.S.; Zhou, S.X. FeSiBPNbCu alloys with high glass-forming ability and good soft magnetic properties. *Intermetallics* **2014**, *54*, 225–231. [CrossRef]

44. Tsepelev, V.; Konashkov, V.; Starodubtsev, Y.; Belozerov, V.; Gaipishevarov, D. Optimum regime of heat treatment of soft magnetic amorphous materials. *IEEE Trans. Magn.* **2012**, *48*, 1327–1330. [CrossRef]

45. Zapperi, S.; Cizeau, P.; Durin, G.; Stanley, H.E. Dynamics of a ferromagnetic domain wall: Avalanches, depinning transition, and the barkhausen effect. *Phys. Rev. B* **1998**, *58*, 6353–6366. [CrossRef]

46. Bitoh, T.; Makino, A.; Inoue, A. Origin of low coercivity of $(Fe_{0.75}B_{0.15}Si_{0.10})_{100-x}Nb_x$ (x = 1–4) glassy alloys. *J. Appl. Phys.* **2006**, *99*, 08F102:1–08F102:3. [CrossRef]

47. Bhattacharya, S.; Lass, E.A.; Poon, S.J.; Shiflet, G.J.; Rawlings, M.; Daniil, M.; Willard, M.A. Magnetic properties and thermal stability of (Fe,Co)-Mo-B-P-Si metallic glasses. *J. Appl. Phys.* **2012**, *111*, 063906:1–063906:8. [CrossRef]

48. Shin, J.; Bae, J.; Kim, H.; Lee, H.; Lee, T.; Lavernia, E.; Lee, Z. Ordering–disordering phenomena and micro-hardness characteristics of B_2 phase in Fe–(5–6.5%) Si alloys. *Mater. Sci. Eng. A* **2005**, *407*, 282–290. [CrossRef]

49. Chen, M. Mechanical behavior of metallic glasses: Microscopic understanding of strength and ductility. *Annu. Rev. Mater. Res.* **2008**, *38*, 445–469. [CrossRef]

50. Lee, J.-C.; Park, K.-W.; Kim, K.-H.; Fleury, E.; Lee, B.-J.; Wakeda, M.; Shibutani, Y. Origin of the plasticity in bulk amorphous alloys. *J. Mater. Res.* **2007**, *22*, 3087–3097. [CrossRef]

51. Cheng, Y.; Cao, A.J.; Sheng, H.; Ma, E. Local order influences initiation of plastic flow in metallic glass: Effects of alloy composition and sample cooling history. *Acta Mater.* **2008**, *56*, 5263–5275. [CrossRef]